



Non-parameterized Numerical Analysis Using the Distinct Lattice Spring Model by Implementing the Duncan–Chang Model

Gao-Feng Zhao¹ · Xin-Dong Wei¹ · Feng Liu¹ · Wei-Bao Liu²

Received: 7 May 2019 / Accepted: 7 January 2020
 © Springer-Verlag GmbH Austria, part of Springer Nature 2020

Abstract

Parameter selection is always a critical issue for the numerical modeling of many geotechnical problems. In this work, an idea of non-parameterized numerical analysis is demonstrated by incorporating tri-axial data as the input into the distinct lattice spring model (DLSM). An automatic parameter acquisition procedure is developed to determine the parameters of a modified Duncan–Chang (DC) model which is implemented in the DLSM through the further development of an incremental DLSM and a fabric stress calculation scheme. These newly developed algorithms are verified against available numerical results and experimental counterparts. Then, the discrete feature of the DC-DLSM is explored and discussed through the numerical modeling of large-scale tri-axial tests and a fracturing test. Finally, a real rockfill dam project is analyzed by using the DC-DLSM with the available tri-axial data as the input, and a reasonable fitting is obtained, which shows the possibility for the numerical modeling of the DLSM with no parameter selection burden.

Keywords Distinct lattice spring model · Duncan–Chang model · Parameter selection · Rockfill dam · Fracturing

List of Symbols

Roman Alphabet

a	The model constant of the Duncan–Chang model
b	The model constant of the Duncan–Chang model
c	The cohesion
D	The dimensionless constant of the Duncan–Chang model
E_i	The initial tangent elastic modulus
E_t	The tangent elastic modulus
f_i	The bond force component
F	The dimensionless constant of the Duncan–Chang model
$\mathbf{F}_{ij}^{n,t}$	The normal interaction forces at t
$\mathbf{F}_{ij}^{n,t-\Delta t}$	The normal interaction forces at $t - \Delta t$
$\mathbf{F}_{ij}^{s,t}$	The shear interaction forces at t

$\mathbf{F}_{ij}^{s,t-\Delta t}$	The shear interaction forces at $t - \Delta t$
$\sum \mathbf{F}_i^{(t)}$	The sum of the forces acting on the particle i
$F_y^T(t)$	The reaction force in the y -direction
G	The dimensionless constant of the Duncan–Chang model
k_n	The normal stiffness
k_s	The shear stiffness
K_i	The dimensionless modulus number of the Duncan–Chang model
l	The bond length
l_i^0	The initial length of the i th bond
L	The length of the cubic specimen
L^*	The effective length of the cubic specimen
m_p	The particle mass
n	The dimensionless modulus exponent of the Duncan–Chang model
\mathbf{n}	The normal unit vector
p_a	The atmospheric pressure
q	The deviatoric stress
q_j^*	The ultimate deviation stress
r_i	The radius of particle i
r_j	The radius of particle j
R_f	The failure ratio
$\mathbf{u}_i^{(t+\Delta t)}$	The displacement of particle i at $(t + \Delta t)$
$\mathbf{u}_i^{(t)}$	The displacement of particle i at t

✉ Gao-Feng Zhao
 gaofeng.zhao@tju.edu.cn

¹ State Key Laboratory of Hydraulic Engineering Simulation and Safety, School of Civil Engineering, Tianjin University, Tianjin, China

² Nanjing Hydraulic Research Institute, Nanjing, China

$\dot{\mathbf{u}}_i$	The velocity of particle i
$\dot{\mathbf{u}}_i^{(t+\Delta t)}$	The velocity of particle i at $(t + \Delta t)$
$\dot{\mathbf{u}}_i^{(t)}$	The velocity of particle i at t
$\dot{\mathbf{u}}_{ij}$	The relative velocity between particle i and particle j
$\dot{\mathbf{u}}_{ij}^n$	The normal relative velocity between particle i and particle j
$\dot{\mathbf{u}}_{ij}^s$	The shear relative velocity between particle i and particle j
$\dot{\mathbf{u}}_j$	The velocity of particle j
u_n	The normal deformation of the springs
u_s	The shear deformation of the springs
u_n^*	The ultimate deformation of the springs
u_s^*	The shear deformation of the springs
$u_x^L(t)$	The average displacement of the cubic left surface in the x -direction
$u_x^R(t)$	The average displacement of the cubic right surface in the x -direction
$u_y^B(t)$	The average displacement of the cubic bottom surface in the y -direction
$u_y^T(t)$	The average displacement of the cubic top surface in the y -direction
$u_z^B(t)$	The average displacement of the cubic back surface in the z -direction
$u_z^F(t)$	The average displacement of the cubic front surface in the z -direction
V	The volume of the computational model
V'	The particle's represented volume
\mathbf{x}_i	The coordinate of particle i
\mathbf{x}_j	The coordinate of particle j
\mathbf{x}_i^0	The initial coordinate of particle i
\mathbf{x}_j^0	The initial coordinate of particle j

Greek Symbols

α	The coefficient of the elastic modulus
α^{3D}	The lattice geometry coefficient
β	The translation coefficient of the weight function
γ	The scaling coefficient of the weight function
ε_1	The axial strain
ε_v	The volumetric strain
ε_x	The strain in the x -direction
ε_y	The strain in the y -direction
ε_z	The strain in the z -direction
$[\dot{\varepsilon}]_{\text{bond}}$	The local strain rate of a spring bond
$[\dot{\varepsilon}]_i$	The strain rate of particle i
$[\dot{\varepsilon}]_j$	The strain rate of particle j
ν_t	The tangent Poisson
ν_t'	The modified tangent Poisson ratio
ν^*	The upper limit of the Poisson ratio
σ_1	The major principal stress
$(\sigma_1 - \sigma_3)_f$	The failure strength

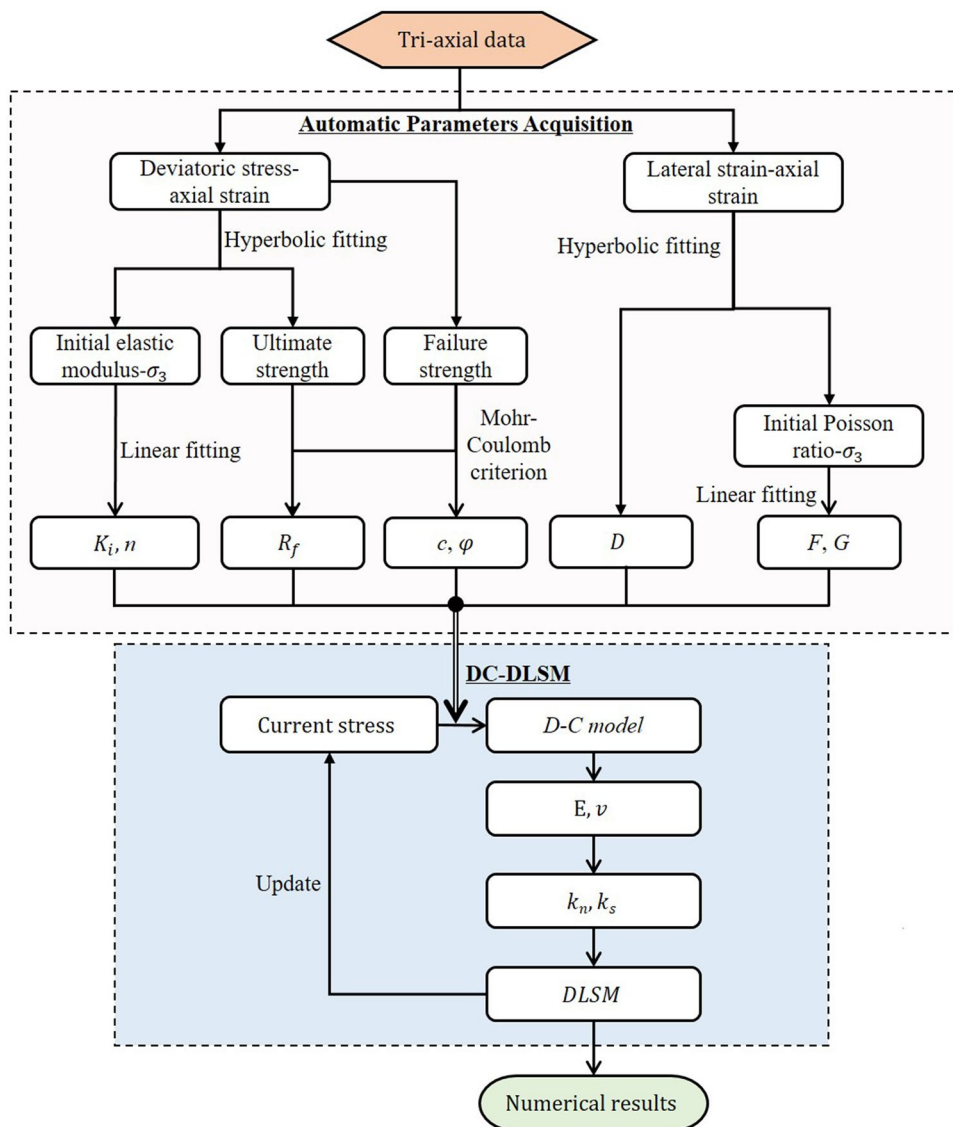
$\sigma_{1,j}^*$	The failure first principle stress
σ_3	The minor principal stress
$\sigma_{3,j}^0$	The confining pressures
σ_{ij}	The stress of the particle
σ_y	The stress in the y -direction
φ	The internal friction angle
χ	The dimensionless damping constant
Δt	The time step
ξ_i	The i th component of the normal vector of the lattice bond
Π	The strain energy
λ	The ratio of horizontal acceleration to gravitational acceleration

1 Introduction

Currently, numerical simulation is generally regarded as the third pillar of scientific study in addition to the traditional experimental and analytical approaches (Abdollahipour et al. 2016; Fan et al. 2013; Kolda 2014). Nevertheless, the parameter selection of numerical modeling in geotechnical applications is still a critical issue that is always being questioned due to the complexity of the rock mass (Yan et al. 2018; Li et al. 2012; Li 2013). The difficulty of selecting parameters handicaps the practical application of the advanced constitutive models (Russell and Khalili 2004; Li et al. 2010, 2013) developed for geomechanics, which usually require many parameters to be determined and might not be robust enough for practical engineering applications (Juang et al. 2018). Moreover, the parameter selection of some discrete models, such as the discrete element model (DEM), is even more complex and a complicated calibration procedure with trial-and-error is usually required (Abdollahipour et al. 2016; Yoon 2007; Kazerani and Zhao 2014), which becomes the main obstacle of their further application in geotechnical engineering. Previous studies have shown that the traditional back analysis (Wang et al. 2007) is generally used to adjust/optimize the input parameters of a numerical model through a minimization of the difference between the numerical results and the field measurement. However, this approach usually requires manual intervention and is still unable to automatically determine the input mechanical parameters for numerical analysis due to the complexity of the calibration between the micro-parameters and the macro-counterparts and the redundancy of the mechanical parameters of the bonded DEM (Liang et al. 2003; Zhao et al. 2018; Zhang et al. 2018; Shi et al. 2019).

In recent years, the lattice spring model (LSM) has received more attention due to its advantage of modeling fracturing. The distinct lattice spring model (DLSM) (Zhao et al. 2011) was initially developed to model the brittle

Fig. 1 Flowchart of NPNA using the DC-DLSM



failure of rock. Later, it was extended to solve coupled hydraulic mechanical problems (Zhao and Khalili 2012), large deformation problems (Zhao 2017), general plasticity problems (Jiang and Zhao 2018; Zhao et al. 2019), etc. The DLSM has taken a step forward in parameter selection, because it has fewer mechanical parameters and is free of parameter calibration, which is attributed to the closed form equation between the micro-parameters and the macro-elastic parameters derived using hyper-elasticity analysis. The input elastic mechanical parameters of the DLSM are the elastic modulus and the Poisson ratio, which are more convenient to be input than the micro-mechanical parameters. Furthermore, it would be convenient and straightforward if we could directly input experimental data rather than a group of material parameters with various definitions. In this work, we refer to this technique as non-parameterized numerical analysis (NPNA). Here, to realize NPNA using the DLSM,

we will directly input deviatoric stress–axial strain and volumetric strain–axial strain curves from tri-axial tests into the DLSM for the numerical analysis of geotechnical problems. The classical DC model developed by Duncan and Chang in 1970 is a suitable candidate for this purpose (Duncan and Chang 1970). Although many advanced constitutive models have been developed, the DC model is still widely used in practical geotechnical engineering projects, especially in China (Guo and Li 2012; Wang et al. 2007; Zhou et al. 2011; Zhang et al. 1999). The major reason is the amount of accumulated data on rock material parameters of the DC model for various rock engineering projects.

The DC model is a well-developed non-linear constitutive model in geomechanics. The corresponding study can be classified into parameter-sensitive investigation (Su et al. 2008; Wang et al. 2004), implementation in special software (Wu et al. 2011; Guo and Li 2012), practical engineering

application (Chen et al. 2011; Kuniyuki et al. 2012; Zhou et al. 2011; Zhang et al. 1999), and parametric back analysis (Wang et al. 2007). The parameter identification of the DC model is relatively straightforward, but the automatic parameter acquisition from the raw data of tri-axial tests is still not well reported. The automatic parameter acquisition is not trivial but an essential step for NPNA using the DC model, which must be mathematically robust and can be easily implemented. Moreover, the DC model is a typical non-linear elastic constitutive model, and the general framework developed for plasticity (Zhao et al. 2019) can not be used for this case. New developments for the DLISM to implement non-linear elasticity are required.

The ultimate target of NPNA is to conduct numerical modeling by directly utilizing raw experimental data such as stress wave curve, penetration versus force curve, stress strain curves of the ultrasonic test, standard penetration tests, and tri-axial tests. NPNA is an integration of automatic back analysis, experimental tests, and numerical modeling. The aim of this paper is to illustrate NPNA using the DLISM, i.e., to directly input the tri-axial compressive test data into the DLISM for the numerical analysis of geotechnical problems. The paper is organized as follows. First, an automatic parameter identification procedure is developed. Through a comparison between model predictions of the original DC model and the experimental counterparts, a modification on the Poisson ratio equation of the DC model is developed, which can result in a better fitting of the experimental data. Then, an incremental DLISM and a fabric stress tensor calculation scheme are developed to implement the DC model into the DLISM. Following this, the DC-DLISM is verified against tri-axial test data of rockfill materials. The results indicate that the DC-DLISM can successfully capture the non-linear mechanical responses of the rockfill materials. Moreover, the DC-DLISM also inherits the advantage of modeling fracturing problems from the original DLISM, which is demonstrated by a notched specimen under tension and the fracturing of a bonded granular dam under horizontal acceleration. Then, the DC-DLISM is used to analyze the settlement of the Roadford Dam in Britain, in which the raw tri-axial compressive data are directly used without any manual parameter calibration procedure. We demonstrate that the NPNA using the DC-DLISM is able to reasonably predict the settlement compared with the field measurement. Finally, some conclusions and discussions are provided.

2 NPNA and DLISM

As shown in Fig. 1, the principle of NPNA is to directly input the tri-axial compressive test data. Then, the required corresponding parameters are automatically calculated, and the numerical analysis is carried out by the DLISM. To the

end user, the steps of the macro- and micro-mechanical parameter calibrations are omitted. There are two main components of the NPNA of the DLISM: (1) the automatic parameter acquisition of the DC model and (2) the DC-DLISM.

2.1 Automatic Parameter Acquisition of the DC Model

As a typical non-linear elastic constitutive model, the DC model has gained great popularity in geotechnical engineering, especially in the numerical analysis of rockfill dams. According to conventional tri-axial compressive tests, the relationship between the deviatoric stress and the axial strain can be described as:

$$\sigma_1 - \sigma_3 = \frac{\varepsilon_1}{a + b\varepsilon_1}, \quad (1)$$

where σ_1 and σ_3 are the maximum and minimum principal stresses, respectively, ε_1 denotes the axial strain, and a and b

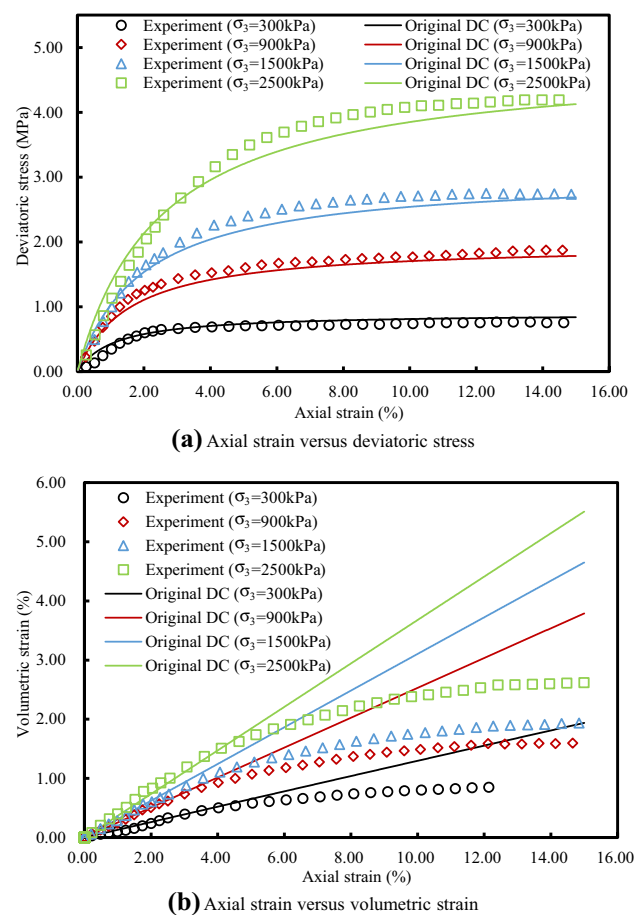


Fig. 2 Comparison of the original DC model and the tri-axial compressive test data for clay (Dong et al. 2013)

are model constants. The macroscopic material parameters of the DC model, such as the elastic modulus and the Poisson ratio, change with the stress state. In this work, we adopt the tangent version of the DC model, in which the tangent elastic modulus E_t and the tangent Poisson ratio ν_t are used to represent the non-linear elastic response of the materials. The tangent elastic modulus can be written as:

$$E_t = E_i \left(1 - \frac{R_f(\sigma_1 - \sigma_3)}{(\sigma_1 - \sigma_3)_f} \right)^2, \tag{2}$$

where

$$E_i = K_i p_a \left(\frac{\sigma_3}{p_a} \right)^n, \tag{3}$$

and E_i is the initial tangent elastic modulus, R_f is the failure ratio with a variable less than 1, $(\sigma_1 - \sigma_3)_f$ denotes the failure strength based on the Mohr–Coulomb failure criterion, K_i is a dimensionless modulus number, p_a denotes the

atmospheric pressure (101.4 kPa), and n is a dimensionless modulus exponent. The tangent Poisson ratio is given as:

$$\nu_t = \frac{G - F \lg \left(\frac{\sigma_3}{p_a} \right)}{(1 - D\Omega)^2}, \tag{4}$$

where

$$\Omega = \frac{(\sigma_1 - \sigma_3)}{K_i p_a \left(\frac{\sigma_3}{p_a} \right)^n \left[1 - \frac{R_f(\sigma_1 - \sigma_3)(1 - \sin\varphi)}{2c \cdot \cos\varphi + 2\sigma_3 \sin\varphi} \right]}, \tag{5}$$

and $G, F,$ and D are dimensionless constants, c denotes the cohesion and φ is the internal friction angle. The DC model only has eight parameters ($c, \varphi, K_i, n, R_f, G, F,$ and D) which can be easily obtained by the tri-axial compressive test. It is assumed that there are tri-axial data for tests conducted at different confining pressures as $(\sigma_{3j}^0)_{j=1, 2, \dots, m}$, and the number of tests m should be larger than two. Each piece of tri-axial test data includes the axial strain (ϵ_1) versus the deviatoric stress (q) curve (ϵ_1, q) and the axial strain (ϵ_1) versus the volumetric strain (ϵ_v) curve (ϵ_1, ϵ_v). As shown in Fig. 1, the automatic parameter acquisition can be divided into two subroutines. The first one is to obtain the parameters that are related to the elastic modulus using the (ϵ_1, q) curves. The first step is to obtain the corresponding coefficients of the hyperbolic function of each curve through non-linear fitting of the experimental data. This will result in an array as $(a_j, b_j)_{j=1, 2, \dots, m}$, which can be used to obtain the initial tangent elastic modulus described as:

$$E_{ij} = \frac{1}{a_j}. \tag{6}$$

Taking the logarithm of both sides of Eq. (3) yields:

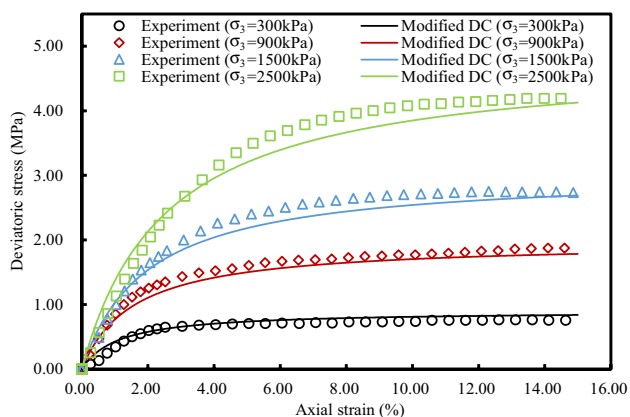
$$\log \left(\frac{E_i}{p_a} \right) = \log (K_i) + n \log \left(\frac{\sigma_3}{p_a} \right). \tag{7}$$

Then, K_i and n can be obtained through a linear fitting over $\left(\log \left(\frac{E_{ij}}{p_a} \right), \log \left(\frac{\sigma_{3j}^0}{p_a} \right) \right)$. For each (ϵ_1, q), we can obtain the failure deviatoric stress as $q_j^* = \max(q)$, and R_f is obtained as:

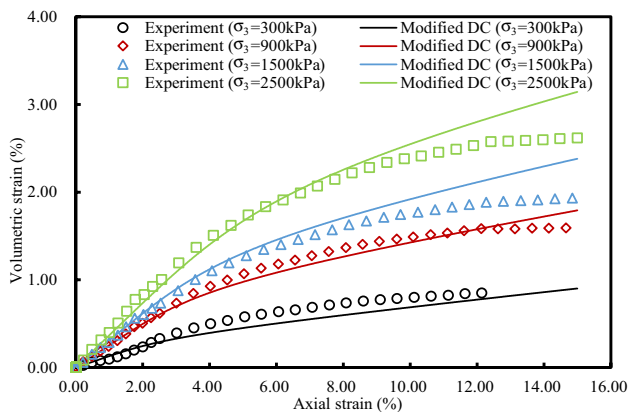
$$R_f = \frac{\sum_{j=1}^m \frac{q_j^*}{b_j}}{m}. \tag{8}$$

The corresponding first principle failure stress of each tri-axial test can be given as:

$$\sigma_{1,j}^* = q_j^* + \sigma_{3j}^0. \tag{9}$$



(a) Axial strain versus deviatoric stress



(b) Axial strain versus volumetric strain

Fig. 3 Comparison of the modified DC model and the tri-axial compressive test data for clay (Dong et al. 2013)

The corresponding parameters c and φ of the Mohr–Coulomb criterion can be obtained by using a linear fitting over $(\sigma_{3,j}^0, \sigma_{1,j}^*)$. Now, all the related parameters of the DC model for calculating the tangent elastic modulus using Eq. (2) are ready. Because only the raw data of the tri-axial compressive tests and linear and non-linear fitting are involved, this process can be automatically performed. A similar procedure can be developed for the parameters involved in Eq. (4) for the tangent Poisson ratio. As an example, the tri-axial compressive data for clay provided by Dong et al. (2013) were processed by the proposed automatic parameter acquisition procedure, as shown in Fig. 1. The corresponding prediction results of the DC model with these parameters are shown in Fig. 2. Good fitting is observed between the axial strain and the deviatoric stress. However, the relationship between the axial strain and the volumetric strain deviates from the experimental data as the axial strain increases. Further observations of the experimental data showed that the corresponding Poisson's ratio is close to 0.5 and is a constant when the axial strain is large enough. In terms of this rule, a new Poisson's ratio function is obtained by modifying the value obtained from the original Poisson's ratio function by setting a weighting function. The basic principle is that it is determined by the original formula at the beginning and gradually transitions to a constant close to 0.5. This feature can be obtained by the weighting function represented by the Sigmoid function, so the final modified function can be obtained, as shown in Eq. (10).

$$v_t' = \left(1 - \frac{1}{1 + e^{(\alpha-\beta)\gamma}}\right)v_t + \frac{1}{1 + e^{(\alpha-\beta)\gamma}}v^*, \quad (10)$$

where v_t' , v_t , and v^* are the modified tangent Poisson ratio, the original tangent Poisson ratio, and the upper limit of the Poisson ratio, respectively, α denotes the coefficient of the elastic modulus, which is defined as the ratio of the tangent elastic modulus to the initial tangent elastic modulus (the range of its value is 0–1), β is the translation coefficient of the weight function, and γ represents the scaling coefficient of the weight function greater than 10. The DC model with further Poisson ratio modifications is called the modified DC model. The corresponding results of the modified DC model are shown in Fig. 3. A better fitting over the volumetric strain is achieved. In actual numerical analyses, these additional parameters, α , β , γ , and v^* , are constants, and the same automatic parameter acquisition procedure as that used in the original DC model can be used. Among these parameters, the trial-and-error method was used to determine the parameters β and γ in this paper: $\beta=0.08$, $\gamma=18$, and v^* should be less than 0.5 based on the generalized Hooke's law. Here, we set v^* to 0.42 for numerical stability.

2.2 DC-DLSM

The DLSM (Zhao et al. 2011) is made up of particles connected by bonds composed of normal and shear springs between their centre points. The original DLSM was designed for the dynamic fracturing of brittle solids and was developed initially under total deformation. In this work, to implement the non-linear elasticity model, an incremental version of the DLSM will be developed. The particle velocities rather than the particle displacements will be used to calculate the interaction forces between particles. The implementation of the DC-DLSM is shown in Fig. 1. The normal force between two particles is defined as:

$$\mathbf{F}_{ij}^{n,t} = \begin{cases} \mathbf{F}_{ij}^{n,t-\Delta t} + \hat{k}_n \hat{\mathbf{u}}_{ij}^n \Delta t, & u_n < u_n^* \\ \mathbf{0}, & \text{else} \end{cases}, \quad (11)$$

where $\mathbf{F}_{ij}^{n,t}$ and $\mathbf{F}_{ij}^{n,t-\Delta t}$ are the normal interaction forces at times t and $t - \Delta t$, respectively, \hat{k}_n is the tangent normal stiffness, $\hat{\mathbf{u}}_{ij}^n$ is the normal relative velocity between two particles, Δt is the time step, u_n is the current normal deformation between two particles, and u_n^* is the ultimate normal deformation between two particles that can represent the fracture. Following the equation provided in the original DLSM, the tangent normal stiffness can be given as:

$$k_n = \frac{1}{2} \left(\frac{3E_{t,i}}{\alpha^{3D}(1-2v_{t,i})} + \frac{3E_{t,j}}{\alpha^{3D}(1-2v_{t,j})} \right), \quad (12)$$

where $E_{t,i}$ and $E_{t,j}$ are the tangent elastic modulus of particles i and j , which can be obtained by using Eq. (2), $v_{t,i}$ and $v_{t,j}$ are the tangent Poisson ratios of particles i and j calculated by Eq. (10), and α^{3D} is a lattice geometry coefficient. Given the geometric data of the lattice model, α^{3D} can be estimated as:

$$\alpha^{3D} = \frac{\sum (l_i^0)^2}{V}, \quad (13)$$

where l_i^0 is the initial length of the i th bond, and V is the represented volume of the computational model. The current deformation u_n between two particles refers to the deformation of the spring bond which can be calculated as:

$$u_n = l - l^0 = \|\mathbf{x}_j - \mathbf{x}_i\| - \|\mathbf{x}_j^0 - \mathbf{x}_i^0\|, \quad (14)$$

where \mathbf{x}_i^0 and \mathbf{x}_j^0 are the initial coordinates of particle i and particle j , respectively, and \mathbf{x}_i and \mathbf{x}_j are the current coordinates of particle i and particle j , respectively. The relative normal velocity is given as:

$$\hat{\mathbf{u}}_{ij}^n = (\hat{\mathbf{u}}_{ij} \cdot \mathbf{n}), \quad (15)$$

where $\mathbf{n} = (n_x, n_y, n_z)$ is the normal unit vector which means that particle i points to particle j for the spring connecting

particle i and particle j , and $\dot{\mathbf{u}}_{ij}$ is the relative velocity which is calculated as:

$$\dot{\mathbf{u}}_{ij} = \dot{\mathbf{u}}_j - \dot{\mathbf{u}}_i, \tag{16}$$

where $\dot{\mathbf{u}}_i$ and $\dot{\mathbf{u}}_j$ are the velocities of particle i and particle j , respectively. Following the similar principle, the shear interaction between two particles is given as:

$$\mathbf{F}_{ij}^{s,t} = \begin{cases} \mathbf{F}_{ij}^{s,t-\Delta t} + \hat{k}_s \dot{\mathbf{u}}_{ij}^s \Delta t, & u_s < u_s^* \\ \mathbf{0}, & \text{else} \end{cases}, \tag{17}$$

where $\mathbf{F}_{ij}^{s,t}$ and $\mathbf{F}_{ij}^{s,t-\Delta t}$ are the shear interaction forces at times t and $t - \Delta t$, respectively, \hat{k}_s is the tangent shear stiffness, $\dot{\mathbf{u}}_{ij}^s$ is the shear relative velocity between two particles, u_s is the current shear deformation between two particles, and u_s^* is the ultimate shear deformation between two particles. To maintain rotational invariance, the shear relative velocity $\dot{\mathbf{u}}_{ij}^s$ is calculated as:

$$\dot{\mathbf{u}}_{ij}^s = [\dot{\epsilon}]_{\text{bond}} \cdot \mathbf{n}l - (([\dot{\epsilon}]_{\text{bond}} \cdot \mathbf{n}l) \cdot \mathbf{n})\mathbf{n}, \tag{18}$$

where l is the bond length, and $[\dot{\epsilon}]_{\text{bond}}$ is the strain state of the connecting bond, which is evaluated as:

$$[\dot{\epsilon}]_{\text{bond}} = \frac{[\dot{\epsilon}]_i + [\dot{\epsilon}]_j}{2}, \tag{19}$$

where $[\dot{\epsilon}]_i$ and $[\dot{\epsilon}]_j$ are the strains of particle i and particle j , respectively. In this work, the local strain rate of a given particle is obtained using the least square method over the particle velocities of the particle cluster, which is defined as the collection of particles linked to the particle itself. The shear stiffness is given as:

$$k_s = \frac{1}{2} \left(\frac{3(1 - 4\nu_{t,i})E_{t,i}}{\alpha^{3D}(1 + \nu_{t,i})(1 - 2\nu_{t,i})} + \frac{3(1 - 4\nu_{t,j})E_{t,j}}{\alpha^{3D}(1 + \nu_{t,j})(1 - 2\nu_{t,j})} \right). \tag{20}$$

Fig. 4 Geometric model and computational model of the rectangle plate with a side circular notch under tensile loading

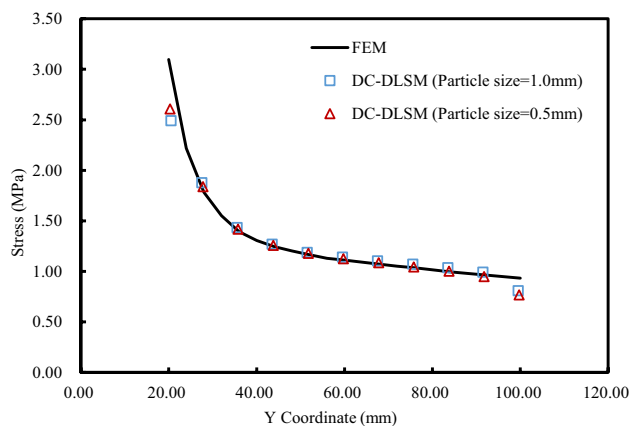
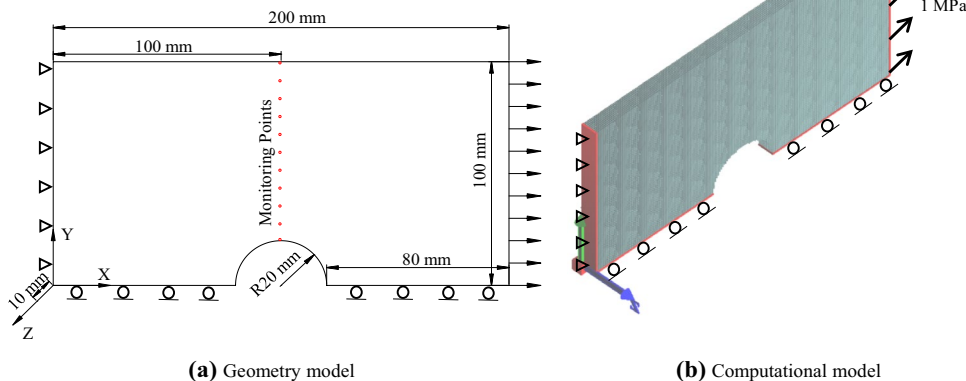


Fig. 5 The stress in the x -direction of the monitoring points in the DC-DLSM and the FEM

With the above equations, the sum forces acting on a particle can be obtained. Using the explicit central finite-difference scheme with a simple variable substitution for the particle velocities to have a half step moving, the particle velocity can be updated as:

$$\dot{\mathbf{u}}_i^{(t+\Delta t)} = \dot{\mathbf{u}}_i^{(t)} + \frac{\sum \mathbf{F}_i^{(t)}}{m_p} \Delta t, \tag{21}$$

where Δt is the time step, $\dot{\mathbf{u}}_i^{(t+\Delta t)}$ is the particle velocity at $(t + \Delta t)$, $\dot{\mathbf{u}}_i^{(t)}$ is the particle velocity at t , $\sum \mathbf{F}_i^{(t)}$ is the sum of forces acting on particle i including applied external forces, and m_p is the particle mass. Finally, the updated displacement can be obtained as:

$$\mathbf{u}_i^{(t+\Delta t)} = \mathbf{u}_i^{(t)} + \dot{\mathbf{u}}_i^{(t+\Delta t)} \Delta t, \tag{22}$$

where $\mathbf{u}_i^{(t+\Delta t)}$ is the displacement at $(t + \Delta t)$ and $\mathbf{u}_i^{(t)}$ is the displacement at t . For static analysis, mechanical damping needs to be taken into account to achieve the force

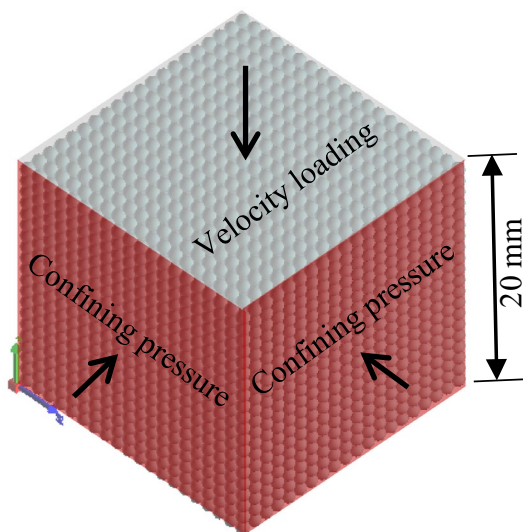


Fig. 6 Computational model of the tri-axial compressive test

equilibrium as soon as possible. By doing so, Eq. (21) can be rewritten as:

$$\dot{\mathbf{u}}_i^{(t+\Delta t)} = \dot{\mathbf{u}}_i^{(t)} + \left\{ \sum \mathbf{F}_i^{(t)} - \chi \left| \sum \mathbf{F}_i^{(t)} \right| \text{sgn}(\dot{\mathbf{u}}_i^{(t)}) \right\} \frac{\Delta t}{m_p}, \quad (23)$$

where χ is the dimensionless damping constant independent of the mechanical properties and boundary conditions ($\chi = 0.6$ in this work). The updated spring bond force can be performed when the elastic modulus and the Poisson ratio are given which are updated using the modified DC model. Using the similar principle of fabric stress calculations of the bonded DEM, the stress of the particle is given as:

$$\sigma_{ij} = \frac{1}{2} \sum \frac{f_i l_j}{V'}, \quad (24)$$

where f_i is the bond force component considering both the normal and shear interactions, l_j denotes the length of the spring bond component, and V' is the particle's represented volume, which is calculated as:

$$V' = \frac{r_i^3}{\sum r_j^3} V, \quad (25)$$

where r_i and r_j are the radii of current particle i and particle j , respectively, and V is the represented volume of the entire

computational model. The proof of Eq. (24) will be derived by using hyper-elasticity. It is noted that one single spring bond will be shared with two particles; therefore, the corresponding strain energy is equally shared. Therefore, for a given particle with its local lattice network, assuming that a simple strain deformation ϵ_{ij} is applied to the particle, its stored strain energy can be given as:

$$\begin{aligned} \Pi &= \frac{1}{2V'} \sum \left(\frac{1}{2} k_n u_n^2 + \frac{1}{2} k_s u_s^2 \right), \\ &= \frac{1}{4V'} \sum l^2 \left(k_n \xi_i \epsilon_{ij} \xi_j \xi_n \epsilon_{nm} \xi_m \right. \\ &\quad \left. + k_s \left((\epsilon_{kl} \xi_l - \xi_i \epsilon_{ij} \xi_j \xi_k) (\epsilon_{km} \xi_m - \xi_n \epsilon_{nm} \xi_m \xi_k) \right) \right), \end{aligned} \quad (26)$$

where k_n is the normal stiffness, k_s is the shear stiffness, and ξ_i is the i th component of the normal vector of the lattice spring bond. Then, the particle stress can be derived using the hyperelastic theory as:

$$\begin{aligned} \sigma_{ij} &= \frac{\partial \Pi}{\partial \epsilon_{ij}} = \frac{1}{2V'} \sum l^2 \left(k_n \xi_i \xi_j \xi_n \epsilon_{nm} \xi_m + k_s (\epsilon_{ik} \xi_k \xi_j - \xi_n \epsilon_{nm} \xi_m \xi_i \xi_j) \right) \\ &= \frac{1}{2V'} \sum l \xi_j (f^n \xi_i + f^s \xi_i) \\ &= \frac{1}{2} \sum \frac{f_i l_j}{V'}. \end{aligned} \quad (27)$$

Unlike the bonded DEM, the calculation of stress requires a measurement sphere to get the average stress; Eq. (24) directly gives the particle stress. The accuracy of Eq. (24) will be verified in the following section. Now, all equations are ready for the NPNA using the DC-DLSM.

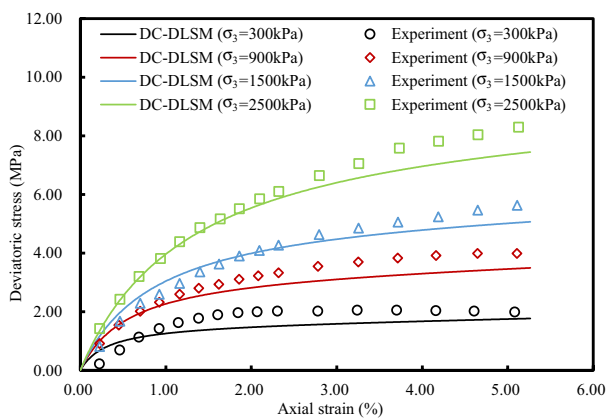
3 Verification

3.1 Elastic Boundary-Value Problems

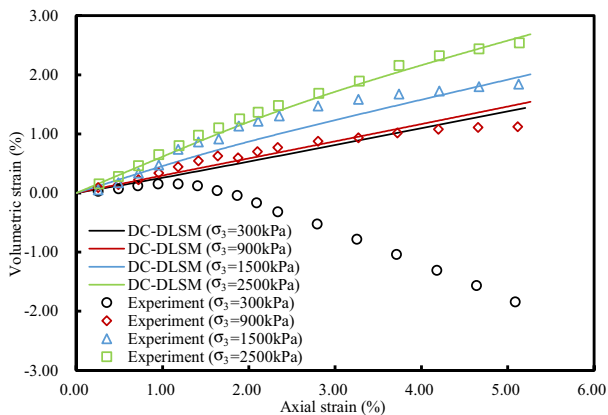
The stress definition stated by Eq. (24) is different from the classical definition in continuum mechanics which is used in the FEM. To check the feasibility of this stress calculation equation and the incremental equations developed for the DLSM, a typical linear elastic boundary-value problem was solved using the DLSM with the elastic modulus and the Poisson ratio set as constants during the calculation. The geometric model and the corresponding computational model of the DLSM are shown in Fig. 4. The dimensions of the model are 200 mm × 100 mm × 10 mm, with a circular

Table 1 DC parameters obtained by automatic parameter acquisition

Material	c (kPa)	φ (°)	K_i	n	R_f	G	F	D
Rockfill I	174.8082	37.9554	3563.1893	0.1837	0.9135	0.7329	0.3794	0.0258
Rockfill II	133.2169	38.1096	4049.4563	0.1601	0.9242	0.7868	0.3837	0.0197
Rockfill III	55.9083	33.0069	975.2387	0.1640	0.9619	0.2105	0.0029	0.1465

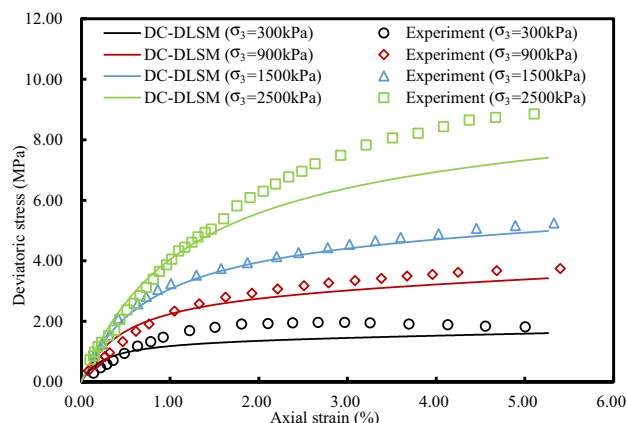


(a) Axial strain versus deviatoric stress

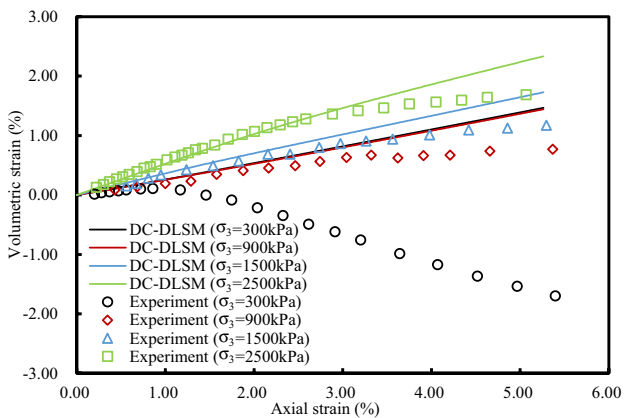


(b) Axial strain versus volumetric strain

Fig. 7 Comparison of the numerical prediction and experimental test results for rockfill I (Dong et al. 2013)



(a) Axial strain versus deviatoric stress



(b) Axial strain versus volumetric strain

Fig. 8 Comparison of the numerical prediction and experimental test results for rockfill II (Dong et al. 2013)

notch with a radius of 20 mm, and monitoring points are put in the middle of the model (see Fig. 4a). A tensile load of 1 MPa is applied to the right side of the model. The stress in the x -direction of the monitoring points is analyzed by the circular orifice model using both the DLSM and the FEM. In addition, two models with particle sizes of 0.5 mm and 1.0 mm are built. The mechanical properties of the simulated model are as follows: elastic modulus 30 GPa, Poisson ratio 0.3, and density 2450 kg/m³. The obtained results are shown in Fig. 5. The stress values obtained by the DLSM and the FEM basically agree with each other, and the smaller the particle diameter is, the higher the accuracy is. It is concluded that the incremental equations and the fabric stress equation for the DLSM are applicable.

3.2 Tri-axial Compressive Test of Rockfill Materials

In this section, the tri-axial compressive tests of rockfill materials are simulated by the DC-DLSM. The corresponding experimental data of two rockfill materials (I and II) are taken from the work of Dong et al. (2013). These tests

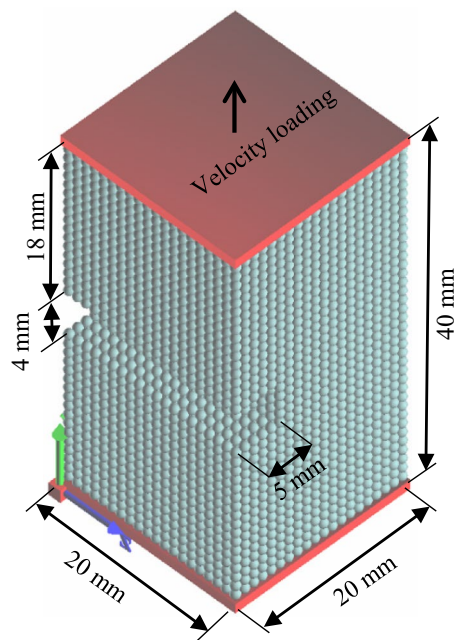


Fig. 9 The model setup and the boundary conditions for the fracturing problem

Fig. 10 The NPNA prediction of the relationship between the loading force and the displacement of the notched specimen under tension and its failure process

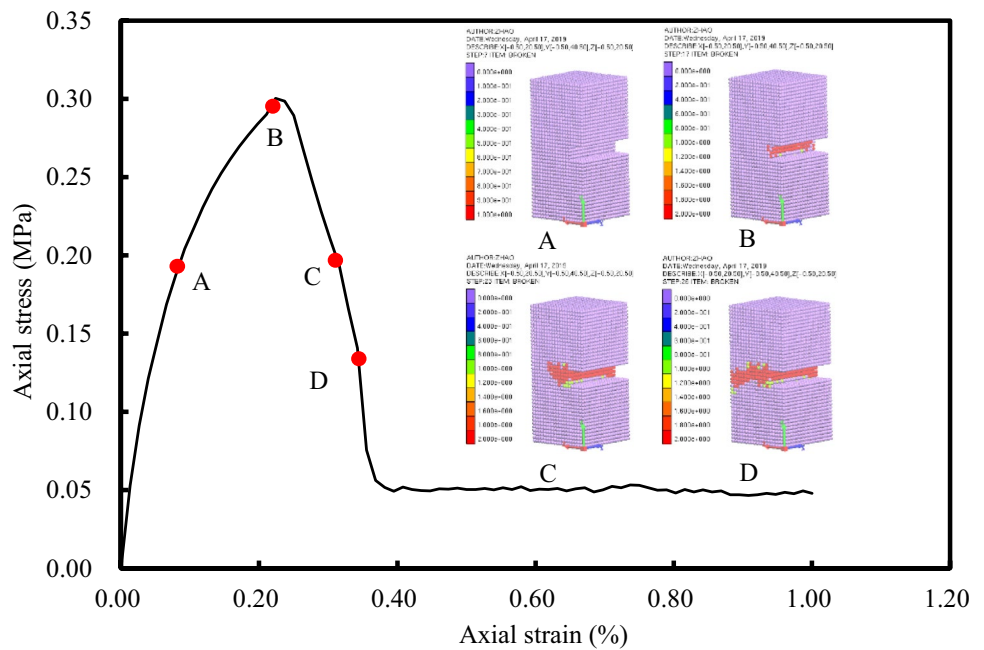
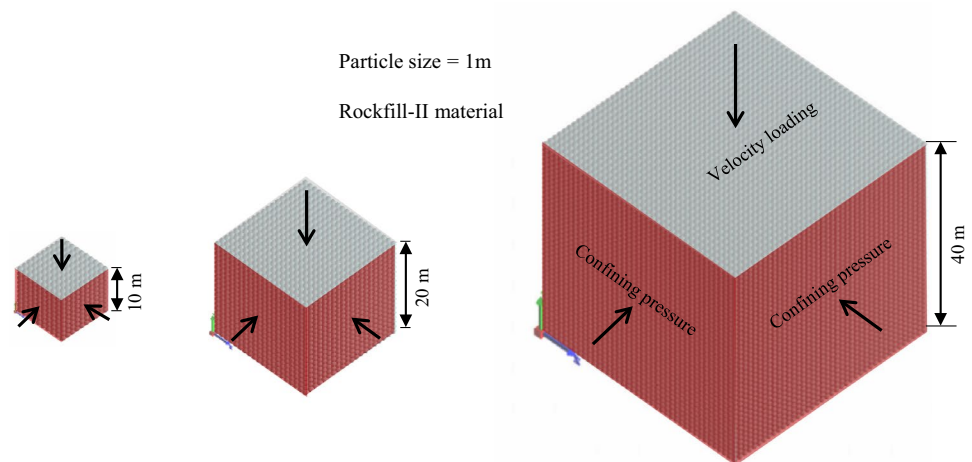


Fig. 11 Computational models with different cube sizes for the large-scale tri-axial compressive test



were conducted at confining pressures of 300 kPa, 900 kPa, 1500 kPa, and 2500 kPa. The computational model with boundary conditions is shown in Fig. 6. A cube with a side length of 20 mm is simulated, and the particle size is 1 mm. The corresponding experimental data are directly input into the numerical model. All the DC parameters obtained by automatic parameter acquisition are listed in Table 1. It is a typical three-dimensional boundary-value problem rather than the elemental test of the constitutive model. Similar to the physical tri-axial test, the stress and strain of the cubic specimen are calculated using the displacement and loading force history recorded in the loading boundaries. The strains are calculated as:

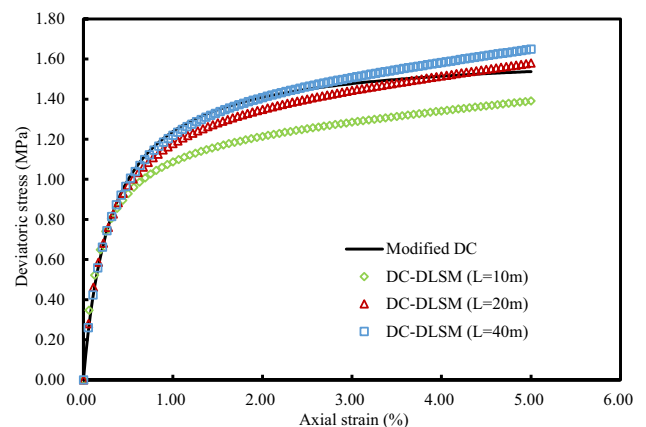
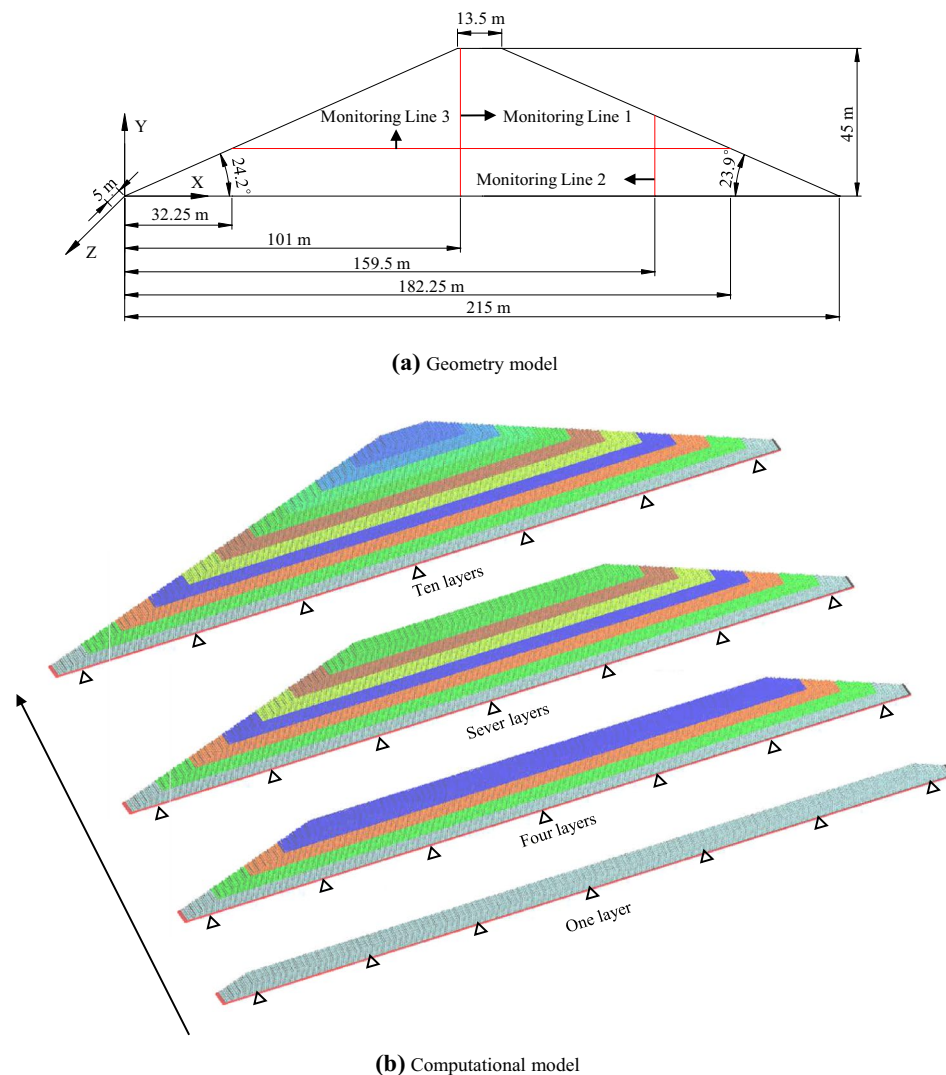


Fig. 12 Numerical results of the DC-DLSM for the large-scale tri-axial compressive tests

Fig. 13 The geometric model and corresponding computational model of the Roadford Dam



$$\epsilon_x = \frac{u_x^R(t) - u_x^L(t)}{L^*}, \tag{28}$$

$$\epsilon_y = \frac{u_y^T(t) - u_y^B(t)}{L^*}, \tag{29}$$

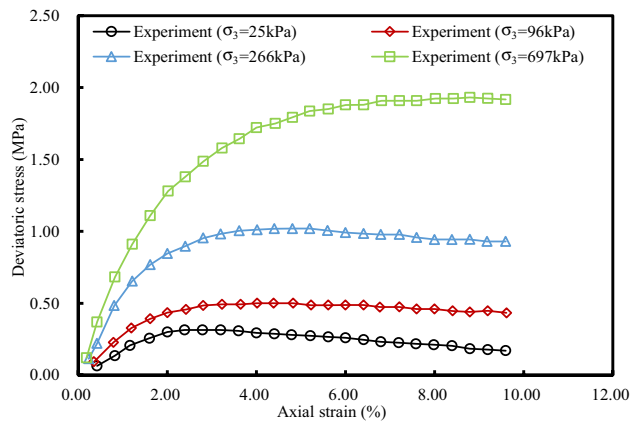
$$\epsilon_z = \frac{u_z^F(t) - u_z^B(t)}{L^*}, \tag{30}$$

where $u_x^R(t)$ and $u_x^L(t)$ are the average displacements in the x -direction of the right and left surfaces of the cubic specimen, respectively, $u_y^T(t)$ and $u_y^B(t)$ are the average displacements in the y -direction of the top and bottom surfaces of the cubic specimen, respectively, $u_z^F(t)$ and $u_z^B(t)$ are the average displacements in the z -direction of the front and back surfaces of the cubic specimen, respectively, and L^*

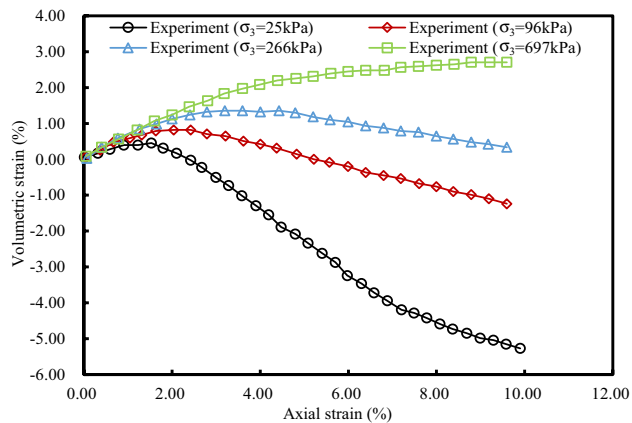
is the effective length of the cubic specimen. The stress is obtained as:

$$\sigma_y = \frac{F_y^T(t)}{L^2}, \tag{31}$$

where $F_y^T(t)$ is the reaction force in the y -direction on the top surface of the cubic specimen, and L is the length of the cubic specimen. The numerical results of the DC-DLSM are plotted in Figs. 7 and 8. The corresponding experimental data are plotted together for comparison. We can conclude that numerical prediction of the relationship between the deviatoric stress and the axial strain can well match the experimental counterparts. However, the DC-DLSM would not provide a good fit over the volumetric strain and the axial strain, especially for the dilation and post-failure stage due to the intrinsic limitations of the DC model in representing volumetric dilation and of the DLSM in representing



(a) Axial strain versus deviatoric stress



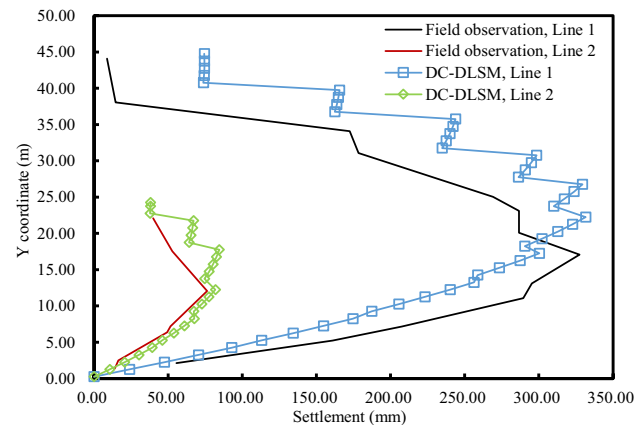
(b) Axial strain versus volumetric strain

Fig. 14 The tri-axial compressive test data of the Roadford Dam (Fu et al. 2018)

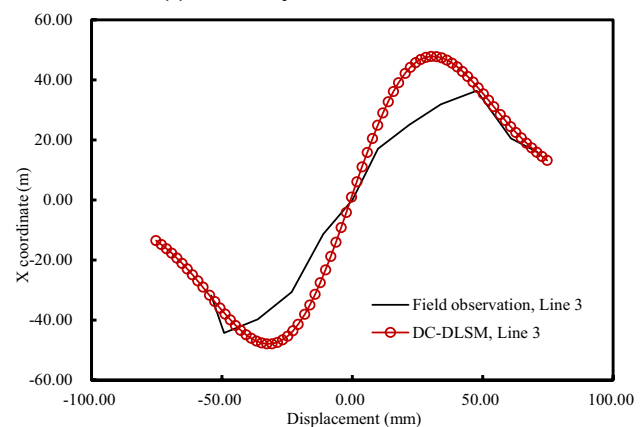
incompressible materials. Similar shortcomings also exist in other numerical methods such as the FEM (Dong et al. 2013; Wang et al. 2017).

4 Discussion

In this section, we will discuss some features of the DC-DLSM. The main advantage of discrete models such as the LSM for rock mechanics is their ability to solve fracturing problems. From Eqs. (11) and (17), it can be seen that the fracturing methodology of the LSM is also inherited in the DC-DLSM. In this paper, the breakage of the corresponding shear spring will occur simultaneously when the normal spring reaches the tensile deformation limit, and vice versa. That is, the corresponding normal spring will also break when the shear spring ruptures. Jiang et al. (2017) only considered the normal spring failure to reconstruct the shape and fracture toughness experiment of type I and mixed crack propagation.



(a) Vertical displacement versus Y coordinate



(b) Horizontal displacement versus X coordinate

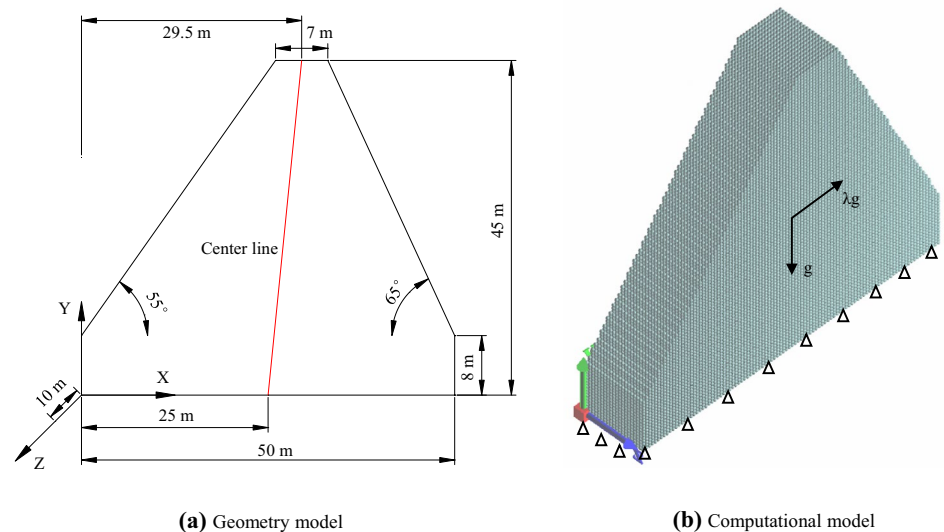
Fig. 15 Numerical results of the monitoring lines compared with field observations

The effect of the shear spring failure on crack propagation is still unclear, so in this paper, we only consider the failure of the normal spring. In the following, one example is conducted to show the features of the DC-DLSM.

4.1 Fracturing of a Notched Specimen

The computational model and boundary conditions of a notched specimen under tension are shown in Fig. 9. The corresponding experimental data of the rockfill material I are provided by Dong et al. (2013). These automatic calculated parameters are also listed in Table 1. In this example, the tensile failure parameter is taken as 0.009 mm to mimic the bonded granular material with a tensile strength of approximately 0.48 MPa. It is possible to replace this tensile failure parameter with the corresponding experimental data such as the uniaxial tension test or the fracture toughness test. The purpose of this example is to show the ability of the DC-DLSM

Fig. 16 The geometric model and the corresponding computational model of the dam



to capture the fracturing process. The automatic tensile failure parameter identification will be our future work. The numerical prediction is shown in Fig. 10. The fractured pattern of a straight line is observed, which is also experimentally observed for the typical notched specimens. This example shows that the DC-DLSM is still able to describe the fracturing problems.

4.2 Influence of Particle Size and Specimen Size

Although the computational power of modern computer has been advanced significantly, it is still insufficient to perform a full-detailed modeling of rockfill dams using discrete models. For example, the previous numerical simulation of tri-axial compressive tests used a particle size of 1 mm. If the same size particles are used in engineering applications, a gigantic number of particles will be generated, which would result in huge computing costs. To check the applicability of NPNA with the DC-DLSM for engineering purpose, three tri-axial compressive numerical tests with side lengths of 10 m, 20 m, and 40 m are conducted under a confining pressure of 300 kPa for the rockfill material II, where the tri-axial experimental data are provided by Dong et al. (2013). The particle size is taken as 1 m, the corresponding computational models are shown in Fig. 11, and all boundary conditions are the same as those in the previous examples. It is noted that a very large-scale tri-axial test is unrealistic due to the cost, so numerical simulation can provide some insights. For example, from the numerical results shown in Fig. 12, we can conclude that the tri-axial test results of a smaller test (e.g., 10 m) would also capture some essential features of the large-scale test (e.g., 40 m). We can also conclude

that the 40 m cube with a particle size of 1 m will show a response similar to that of a 20 mm cube with particle size of 1 mm; therefore, for engineering problems, it would be suitable for the DC-DLSM to use a large particle size to deal with engineering-scale problems.

5 Application

In this section, the feasibility of NPNA based on the modified DC model is further demonstrated by solving two engineering problems.

5.1 Settlement of a Rockfill Dam

The settlement of dams is a very important problem in hydraulic engineering, and the DC model is widely used in the numerical analysis of dam settlement. In this part, taking the Roadford Dam (Hopkins et al. 2010) in Britain as an example, the NPNA based on the modified DC model is used to simulate the dam settlement during construction. As shown in Fig. 13, the geometric model (Hopkins et al. 2010, Fu et al. 2018) and the computational model of the dam are listed, and monitoring lines are put in the middle of the model (see Fig. 13a), where monitoring line 1 and monitoring line 2 are for vertical displacements, and monitoring line 3 is for horizontal displacements. In addition, the entire dam construction process is divided into ten steps from bottom to top (see Fig. 13b) during the numerical modeling; the filling is 4.5 m, and the particle size is 0.5 m. For the stability of the DC model, the initial pressure of the rockfill

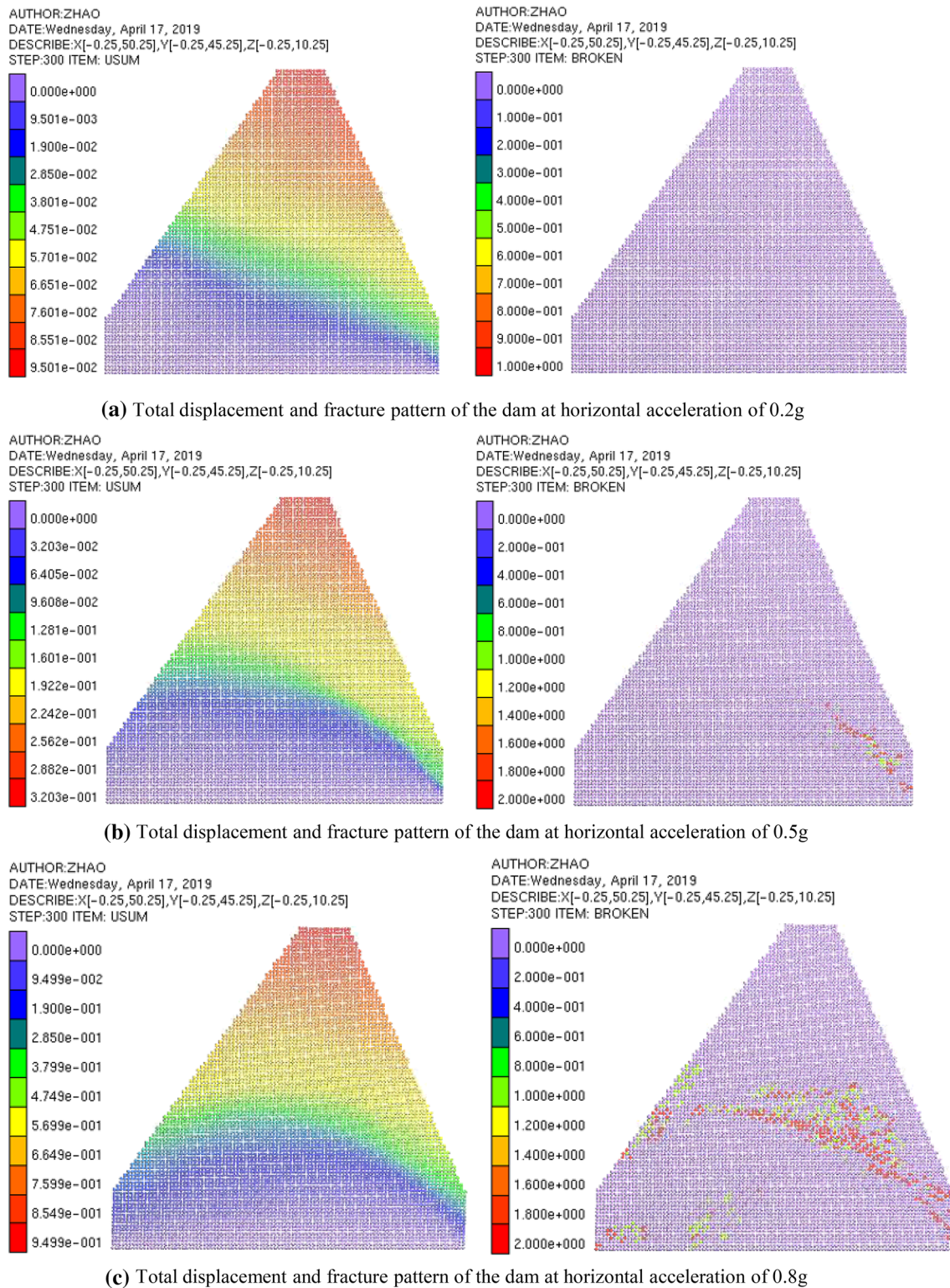


Fig. 17 Numerical results of the dam under earthquakes at different horizontal accelerations

material is taken as 100 kPa (atmospheric pressure). The tri-axial compressive test data of the rockfill material III are available publicly (Fu et al. 2018) and shown in Fig. 14.

Additionally, the automatically calculated parameters are listed in Table 1. Figure 15 shows the numerical results of the DC-DLSM compared with

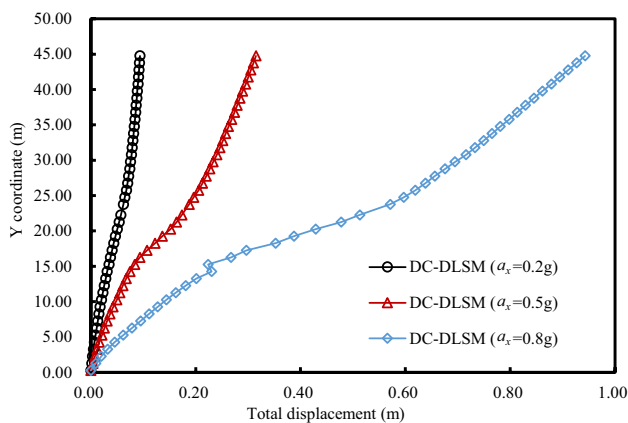


Fig. 18 Settlement on centre line of the dam under earthquakes at different horizontal accelerations

the field observations (Fu et al. 2018). It can be concluded that the DC-DLSM can be used to predict the dam settlement and horizontal displacement during the construction of the rockfill dam.

5.2 Fracturing of a Bonded Granular Dam

To further show the ability of the DC-DLSM to model fracturing, a bonded granular dam under earthquakes is simulated. The applied loadings are vertical gravitational acceleration and horizontal acceleration. To mimic different earthquake magnitudes, the horizontal acceleration is equal to λ times the gravitational acceleration, e.g., 0.2 g, 0.5 g, and 0.8 g. In this paper, the quasi-static method is used to consider the effects of earthquake loads. As shown in Fig. 16, the geometric model and the corresponding computational model of the bonded granular dam are described, where the tri-axial compressive test data of rockfill material I provided by Dong et al. (2013) are used, and the particle size is 0.5 m. Moreover, the monitoring line is put into the middle of the dam to detect the total displacements of the centre line of the dam. The fracture parameter is estimated to be 0.02 m to characterize a tensile strength of approximately 0.67 MPa. The corresponding results are shown in Figs. 17 and 18. It can be seen that the bonded granular dam would fail from the dam heel when the horizontal acceleration reaches 0.5 g and is more serious at 0.8 g. Moreover, with the increase of the magnitude, the total displacements of the centre line of the dam increase sharply. This example demonstrates the applicability of the DC-DLSM for solving fracturing problems.

6 Conclusions

In this work, a preliminary solution called NPNA is developed to solve the parameter selection problem in discrete numerical models. The NPNA is realized by the

implementation of the DC model into the DLSM. An automatic parameter identification procedure is developed. The applicability of this new procedure and additional modification are conducted to ensure the overall performance of the DC model, which results in a modified DC model. The original DLSM is also tailored to an incremental form with a particle stress calculation scheme using the fabric stress rather than the Cauchy stress. From a number of numerical examples, we concluded that the incremental DLSM and the implementation of the DC model are feasible and numerically stable. Moreover, the DC-DLSM also inherits both the advantages on solving fracturing problems from the DLSM and modeling the non-linear response of geomaterials from the DC model. The applicability of using a large particle-size discrete model for engineering problems is also demonstrated. We concluded that with proper model parameters, a discrete model is also suitable for analyzing macroscopic engineering problems. Compared with the continuum-based model, the discrete model might be more feasible for solving fracturing problems. Nevertheless, the DC-DLSM still fails to predict the lateral deformation of materials with dilation and incompressibility. Therefore, further research will include the development of a more generalized method for parameter selection and a more advanced constitutive model for the DLSM.

Acknowledgements This research is financially supported by the National Key R&D Program of China (under # 2018YFC0406800) and National Natural Science Foundation of China (Grant no. 11772221).

References

- Abdollahipour A, Marji MF, Bafghi AY, Gholamnejad J (2016) DEM simulation of confining pressure effects on crack opening displacement in hydraulic fracturing. *Int J Min Sci Tech* 26(4):557–561
- Chen YF, Hu R, Lu WB, Li DQ, Zhou CB (2011) Modeling coupled processes of non-steady seepage flow and non-linear deformation for a concrete-faced rockfill dam. *Comput Struct* 89(13–14):1333–1351
- Dong W, Hu L, Yu YZ, Lv H (2013) Comparison between Duncan and Chang's EB model and the generalized plasticity model in the analysis of a high earth-rockfill dam. *J Appl Math* 20:1–12
- Duncan JM, Chang CY (1970) Nonlinear analysis of stress and strain in soils. *J Soil Mech Found Div* 96(SM5):1629–1653
- Fan LF, Yi XW, Ma GW (2013) Numerical manifold method (NMM) simulation of stress wave propagation through fractured rock mass. *Int J Appl Mech* 5(02):1350022
- Fu M, Hu ZF, Yuan J (2018) Comparative study on deformation analysis of rockfill dam with two models. *Energy Res Manag* 37(04):61–64 (in Chinese)
- Guo PY, Li WC (2012) Development and implementation of Duncan–Chang constitutive model in GeoStudio2007. *Proced Eng* 31(1):395–402
- Hopkins JK, Reid JM, Mccarey J, Bray C (2010) Roadford Dam—20 years of monitoring—managing dams challenges in a time of change. Thomas Telford Ltd, London, pp 187–198

- Jiang C, Zhao GF (2018) Implementation of a coupled plastic damage distinct lattice spring model for dynamic crack propagation in geomaterials. *Int J Numer Anal Methods* 42(4):674–693
- Jiang C, Zhao GF, Khalili N (2017) On crack propagation in brittle material using the distinct lattice spring model. *Int J Solids Struct* 118–119:41–57
- Juang CH, Gong WP, Martin JR, Chen QS (2018) Model selection in geological and geotechnical engineering in the face of uncertainty—does a complex model always outperform a simple model? *Eng Geol* 242:184–196
- Kazerani T, Zhao J (2014) A microstructure-based model to characterize micromechanical parameters controlling compressive and tensile failure in crystallized rock. *Rock Mech Rock Eng* 47(2):435–452
- Kolda T (2014) What kind of science is computational science? A rebuttal. <https://sinews.siam.org/Details-Page/what-kind-of-science-is-computational-science-a-rebuttal>
- Kuniyuki M, Norio T, Kazuo A, Tsutoma Y (2012) A nonlinear elastic model for triaxial compressive properties of artificial methane-hydrate-bearing sediment samples. *Energies* 5:4057–4075
- Li JC (2013) Wave propagation across non-linear rock joints based on time-domain recursive method. *Geophys J Int* 193(2):970–985
- Li JC, Ma GW, Zhao J (2010) An equivalent viscoelastic model for rock mass with parallel joints. *J Geophys Res-Sol Earth* 115:B3
- Li JC, Li HB, Ma GW, Zhao J (2012) A time-domain recursive method to analyse transient wave propagation across rock joints. *Geophys J Int* 188(2):631–644
- Li JC, Li HB, Ma GW, Zhou YX (2013) Assessment of underground tunnel stability to adjacent tunnel explosion. *Tunn Undergr Sp Tech* 35:227–234
- Liang YC, Feng DP, Liu GR, Yang XW, Han X (2003) Neural identification of rock parameters using fuzzy adaptive learning parameters. *Comput Struct* 81(24–25):2373–2382
- Russell AR, Khalili N (2004) A bounding surface plasticity model for sands exhibiting particle crushing. *Can Geotech J* 41(6):1179–1192
- Shi C, Yang WK, Yang JX, Chen X (2019) Calibration of micro-scaled mechanical parameters of granite based on a bonded-particle model with 2D particle flow code. *Granul Matter* 21(2):38
- Su JB, Shao GJ, Chu WJ (2008) Sensitivity analysis of soil parameters based on interval. *Appl Math Mech* 29(12):1651–1662
- Wang ZL, Song MT, Yin ZZ (2004) Analyses of parameters sensitivity of Duncan–Chang model in settlement calculation of embankment. *Rock Soil Mech* 25(7):1135–1138 (in Chinese)
- Wang ZL, Li YC, Shen RF (2007) Correction of soil parameters in calculation of embankment settlement using BP network back-analysis model. *Eng Geol* 91(2–4):168–177
- Wang ZJ, Liu XR, Yang X, Fu Y (2017) An improved Duncan–Chang constitutive model for sandstone subjected to drying-wetting cycles and secondary development of the model in FLAC3D. *Arab J Sci Eng* 42(3):1265–1282
- Wu HM, Shu YM, Zhu JG (2011) Implementation and verification of interface constitutive model in FLAC3D. *Water Sci Eng* 4(3):305–316
- Yan C, Jiao Y-Y, Zheng H (2018) A fully coupled three-dimensional hydro-mechanical finite discrete element approach with real porous seepage for simulating 3D hydraulic fracturing. *Comput Geotech* 96:73–89
- Yoon J (2007) Application of experimental design and optimization to PFC model calibration in uniaxial compression simulation. *Int J Rock Mech Min* 44(6):871–889
- Zhang M, Song E, Chen Z (1999) Ground movement analysis of soil nailing construction by three-dimensional (3-D) finite element modeling (FEM). *Comput Geotech* 25(4):191–204
- Zhang ZH, Deng JH, Zhu JB (2018) A rapid and nondestructive method to determine normal and shear stiffness of a single joint based on 1D wave-propagation theory. *Geophysics* 83(1):WA89–WA100
- Zhao GF (2017) Developing a four-dimensional lattice spring model for mechanical responses of solids. *Comput Method Appl Mech* 315:881–895
- Zhao GF, Khalili N (2012) A lattice spring model for coupled fluid flow and deformation problems in geomechanics. *Rock Mech Rock Eng* 45(5):781–799
- Zhao GF, Fang J, Zhao J (2011) A 3D distinct lattice spring model for elasticity and dynamic failure. *Int J Numer Anal Methods* 35(8):859–885
- Zhao GF, Yin Q, Russell AR, Li YC, Wu W, Li Q (2018) On the linear elastic responses of the 2D bonded discrete element model. *Int J Numer Anal Methods* 43(1):166–182
- Zhao GF, Lian J, Russell A, Khalili N (2019) Implementation of a modified Drucker–Prager model in the lattice spring model for plasticity and fracture. *Comput Geotech* 107:97–109
- Zhou W, Hua JJ, Chang XL, Zhou CB (2011) Settlement analysis of the Shuibuya concrete-face rockfill dam. *Comput Geotech* 38(2):269–280

Publisher's Note Springer Nature remains neutral with regard to jurisdictional claims in published maps and institutional affiliations.